Supporting Information

Metal-Organic Frameworks for the removal of the emerging contaminant atenolol under real conditions

Sara Rojas,[a] Jorge A. R. Navarro,[b] and Patricia Horcajada.[a,]*

[a] Advanced Porous Materials Unit (APMU), IMDEA Energy. Av. Ramón de la Sagra 3, 28935 Móstoles-Madrid, Spain.

[b] Departamento de Química Inorgánica, Universidad de Granada, Av. Fuentenueva S/N, 18071 Granada, Spain.

Table on Contents

S1. Analysis and Characterization

Physicochemical characterization. Fourier transform infrared (FTIR) spectroscopic analyses were performed in a Thermo Scientific Nicolet 6700 FTIR spectrometer using KBr pellets that were dried overnight. N_2 isotherms were obtained at 77 K using Belsorp Max (Bel, Japan). Routine X-ray powder diffraction (XRPD) patterns were collected using a conventional high resolution D5000 Siemens X'Pert MDP diffractometer (θ-2θ) using λ_{Cu} $K_{\alpha1}$, and $K_{\alpha2}$ radiation (λ = 1.54051 and 1.54433 Å), from 5 to 35 (2θ), a step size of 0.02º, and 2 s·step^{-1} in continuous mode, and a conventional PANalytical Empyrean powder diffractometer (PANalytical Lelyweg, Netherlands, θ-2θ) using the same λ_{Cu} $K_{\alpha1}$, and $K_{\alpha2}$ radiation. Thermogravimetric analyses (TGA) were performed using a Perkin-Elmer Diamond TGA/DTA STA 6000 running from room temperature (RT) to 600 ºC with a heating rate of 2 ºC·min^{-1}. The particle size and ζ-potential determinations were performed using a Malvern Nano-ZS, Zetasizer Nano Series. *Ca.* 1 mg of material was dispersed in 10 mL of Milli-Q water using an ultrasound tip (Digital Sonifer 450, Branson; 10%) of amplitude and for 30 s. Transmission electron microscopy (TEM) was performed using a STEM PHILIPS CM20 HR microscope equipped with an energy-dispersive X-ray spectrometer (EDX) operating at an accelerating voltage of 200 keV and a HAADF FEI TITAN G2 microscope also equipped with an EDX. Samples were prepared by dispersing a small amount of the material (*ca.* 3 mg) in absolute ethanol (1 mL) followed by sonication for 10 min and deposition on a copper grid.

High performance liquid chromatography (HPLC). The amount of adsorbed At, as well as the potential release of the corresponding organic linkers were determined using a reversed phase HPLC Jasco LC-4000 series system, equipped with a PDA detector MD-4015 and a multisampler AS-4150 controlled by ChromNav software (Jasco Inc, Japan). A Purple ODS reverse-phase column (5 µm, 4.6 x 150 mm, Análisis Vínicos) was employed. For the quantification of all the chemical species, isocratic conditions were used. The flow rate was 1 mL·min^{-1}, and the column temperature was fixed at 25 ºC. In all cases, the injection volume was 30 µL. The mobile phase was based on a mixture of 50:50 MeOH:phosphate buffered solution (PBS; 0.04 M, pH = 2.5) for MOFs ligands analysis, with different retention time (rt) and absorption maximum (λ) for each molecule: H_2BDC (rt = 3.98 min, λ = 240 nm), H_2BDC-NH_2 (rt = 3.03 min, λ = 228 nm), H_2BDC-$(OH)_2$ (rt = 2.92 min, λ = 217 nm), H_2BDP (rt = 4.00 min, λ = 205 nm), H_2BDP-NH_2 (rt = 2.51 min, λ = 225 nm), H_4-TazBz (rt = 16.36 min, λ = 311 nm), and H_6-TzGal (rt = 3.24 min, λ = 360 nm). At was analyzed using a mixture of 10:90

acetonitrile:phosphate buffered solution (0.04 M: pH = 2.5), rt = 4.81 min and λ = 227 nm. (SI, Section 1).

Preparation of the phosphate buffered solution (0.04 M, pH = 2.5): 0.02 mol (2.4 g) of NaH_2PO_4 and 0.02 mol (2.84 g) of Na_2HPO_4 were dissolved in 1 L of Milli-Q water. The pH was then adjusted to 2.5 with H_3PO_4 (≥ 85%).

S2. HPLC conditions

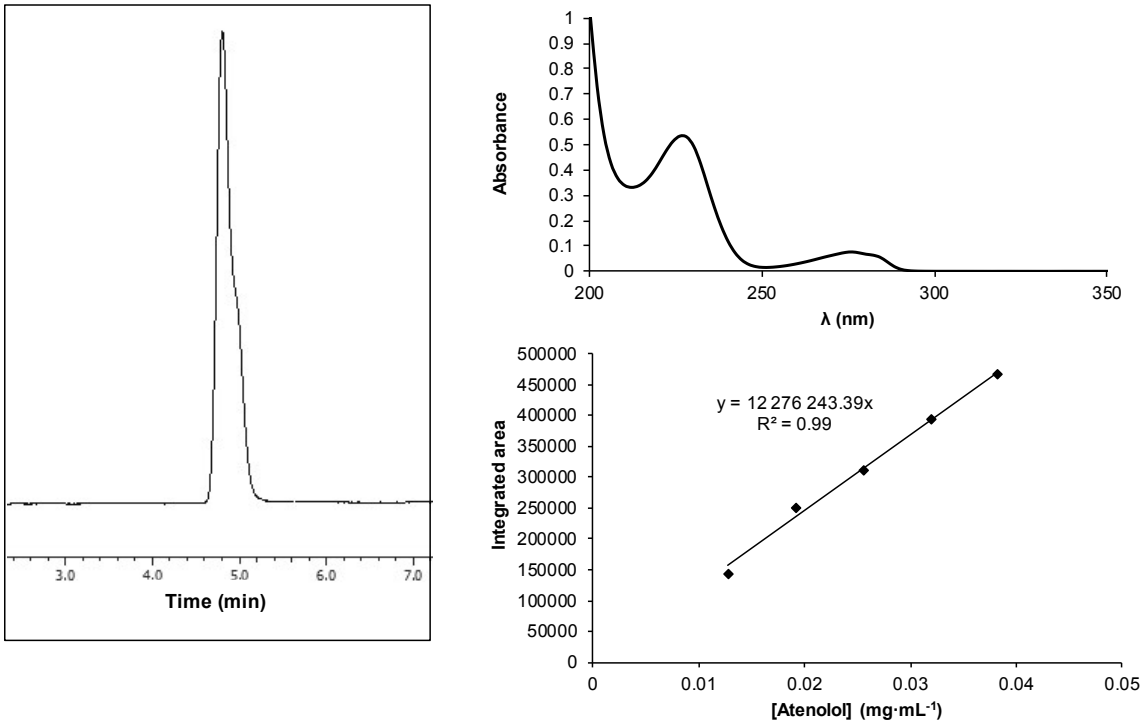

Figure S1. Standard calibration plot by HPLC, and typical UV-vis spectrum and chromatogram of At.

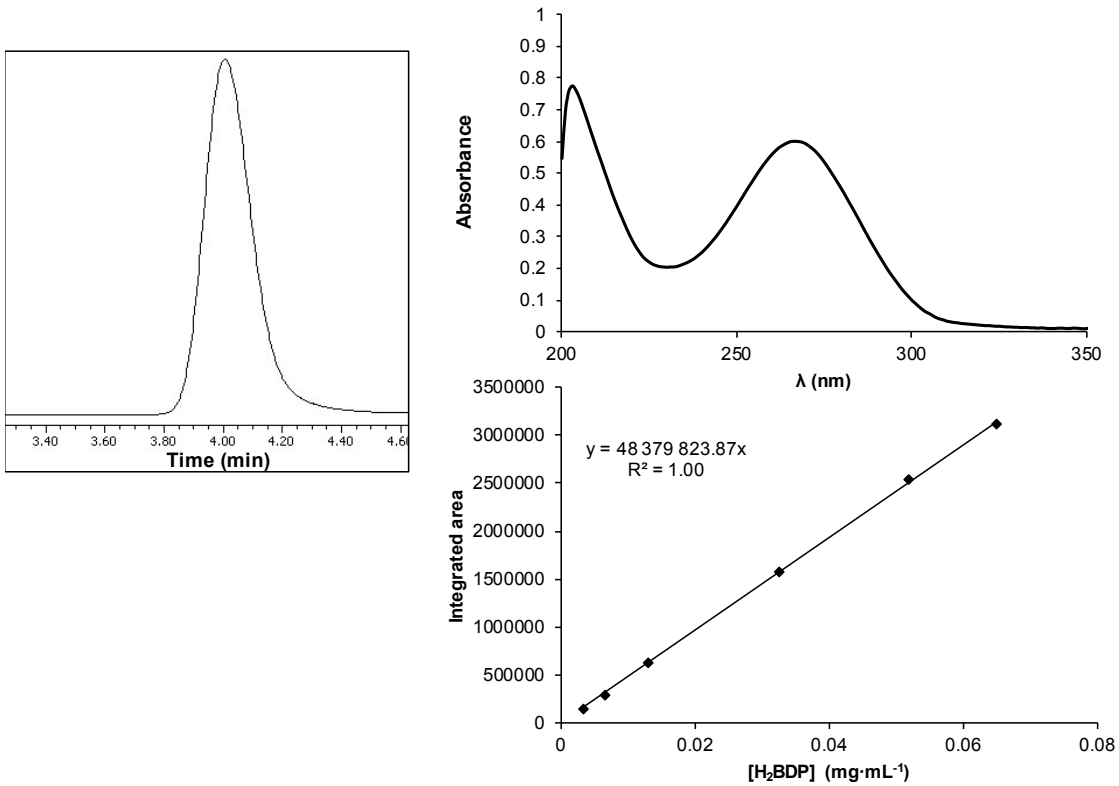

Figure S2. Standard calibration plot by HPLC, and characteristic UV-vis spectrum and chromatogram of H_2BDP.

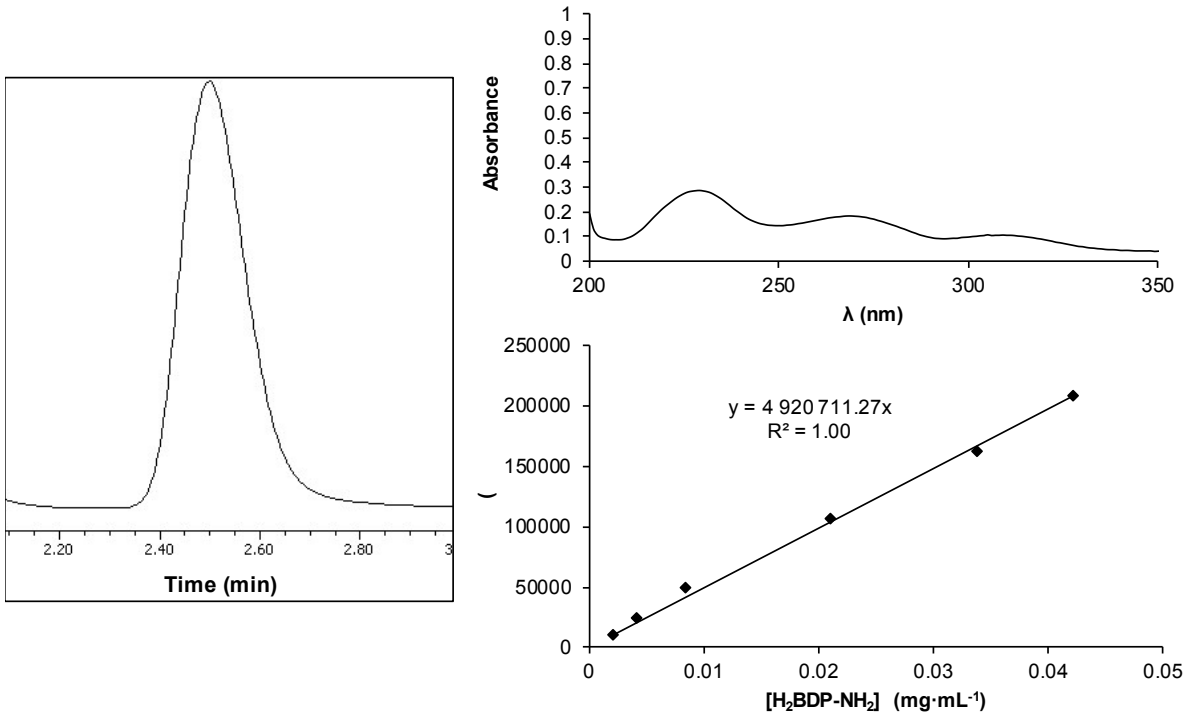

Figure S3. Standard calibration plot by HPLC, and characteristic UV-vis spectrum and chromatogram of H_2BDP-NH_2.

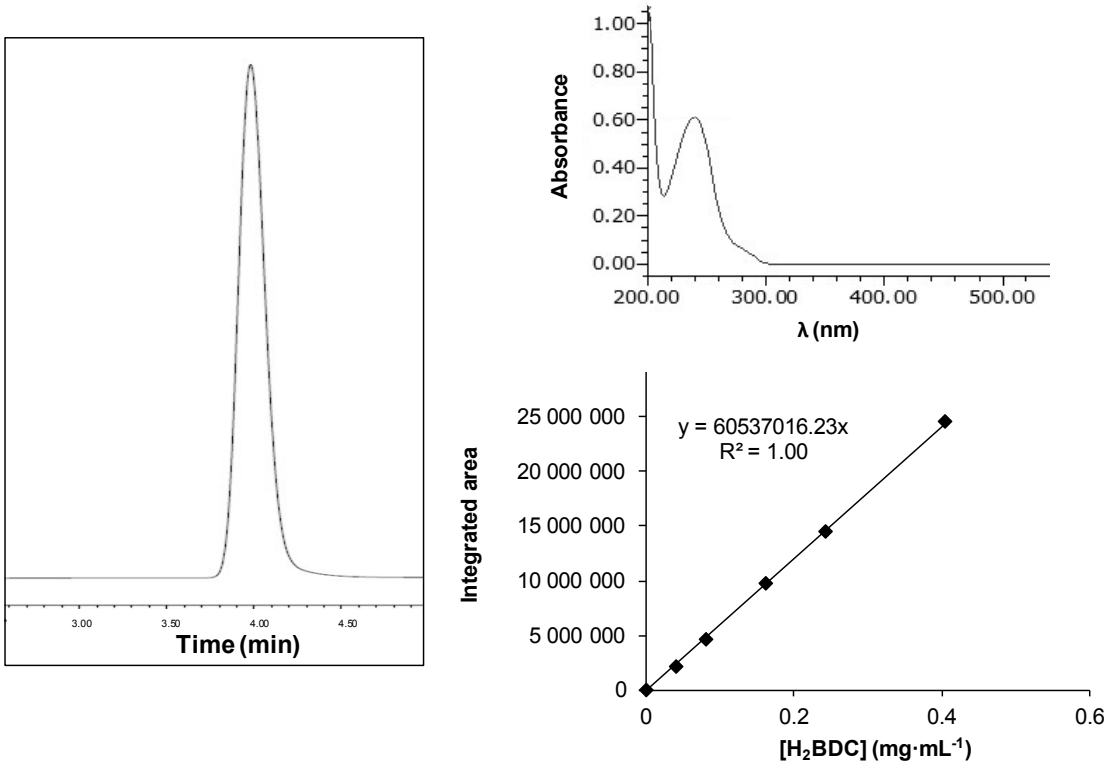

Figure S4. Standard calibration plot by HPLC, and typical UV-vis spectrum and chromatogram of H_2BDC.

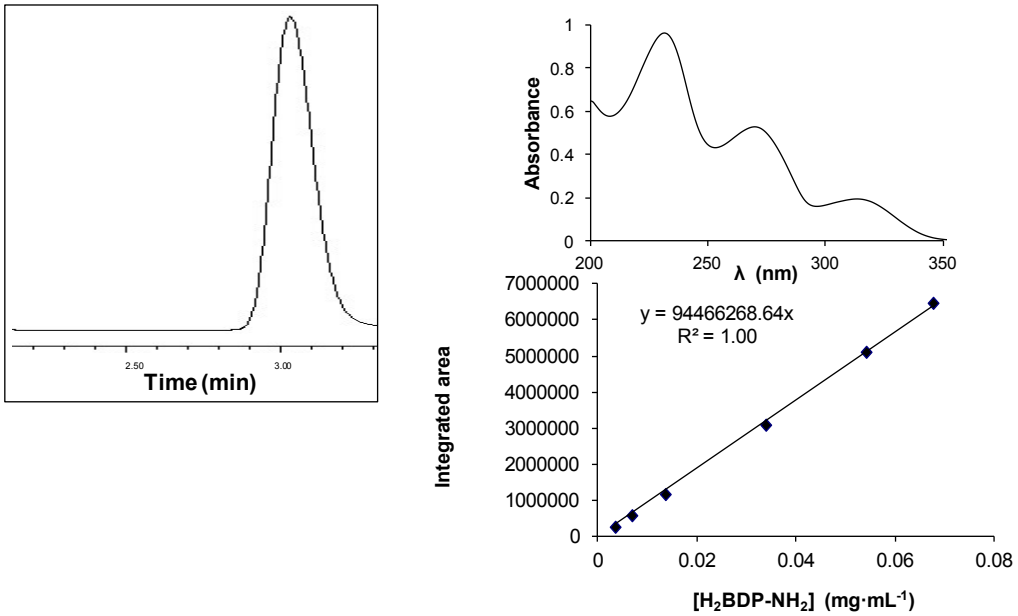

Figure S5. Standard calibration plot by HPLC method, and characteristic UV-vis spectrum and chromatogram of $H_2BDC\text{-}NH_2$.

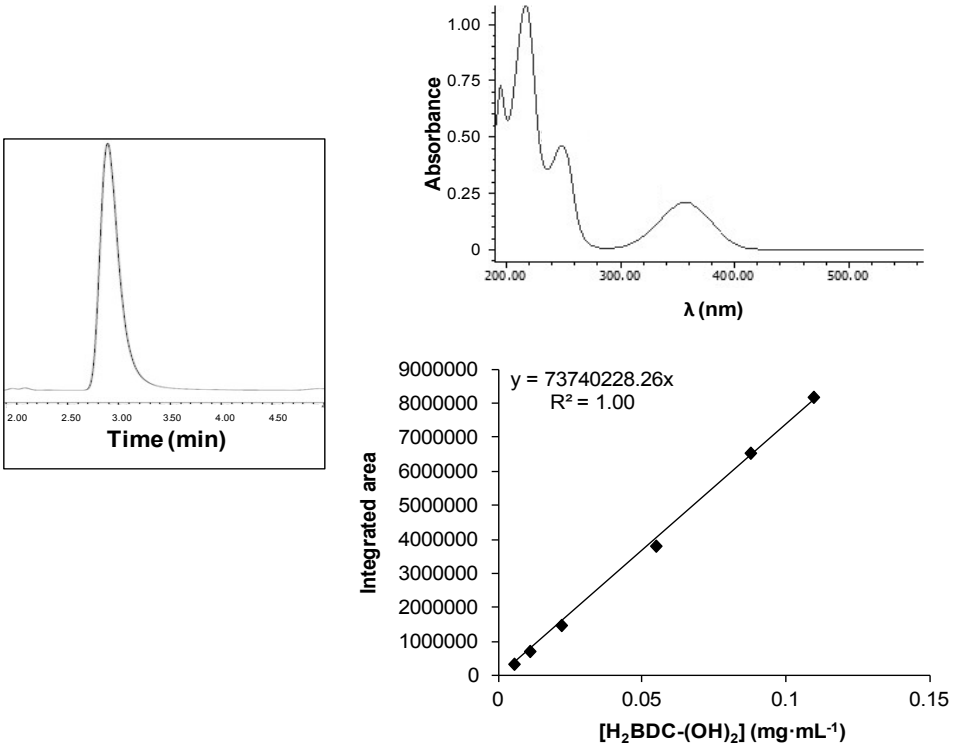

Figure S6. Standard calibration plot by HPLC method, and characteristic UV-vis spectrum and chromatogram of $H_2BDC\text{-}(OH)_2$.

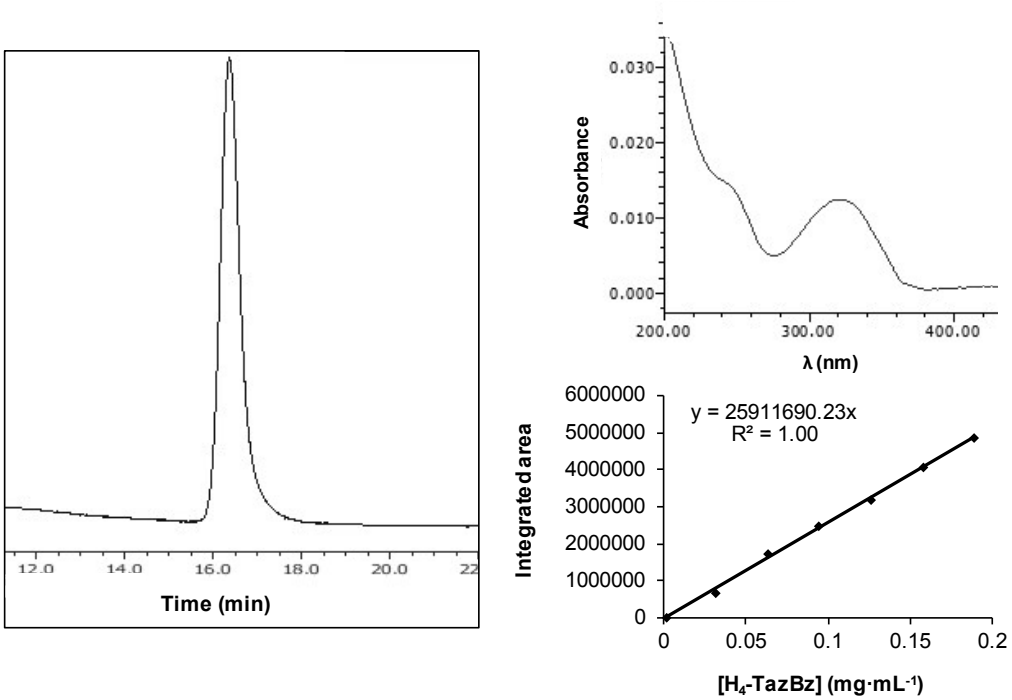

Figure S7. Standard calibration plot by HPLC method, and characteristic UV-vis spectrum and chromatogram of H_4-TazBz.

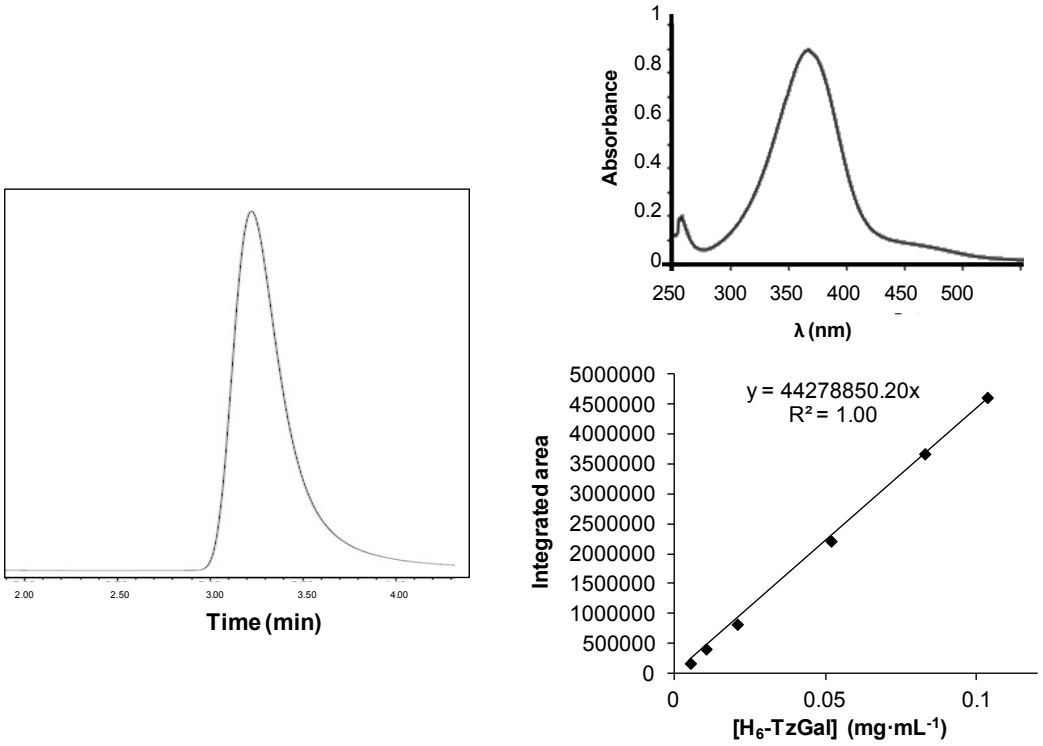

Figure S8. Standard calibration plot by HPLC method, and characteristic UV-vis spectrum and chromatogram of H_6-TzGal.

S3. Synthesis of MOFs

All reactants were commercially obtained and used without further purification. The 1,4-bis(1H-pyrazol-4-yl)benzene ligand (H_2BDP) and its amino derivative ($H_2BDP\text{-}NH_2$),[1–3] the 5,5'-(1,2,4,5-tetrazine-3,6-diyl)bis(benzene-1,2,3-triol) ligand (H_6-TzGal),[4] and the 3,3',5,5'-azobenzenetetracarboxylic acid ligand (H_4-TazBz)[5] were prepared as previously described in literature. The synthesis of starting porous materials was performed following similar procedures to previously reported ones.

Ni_8BDP_6 and $Ni_8(BDP\text{-}NH_2)_6$ or $[Ni_8(OH)_4(H_2O)_2(C_{12}H_7N_4X)_6]\cdot n(H_2O)$, X = H ($Ni_8BDP_6$) or NH_2 ($Ni_8(BDP\text{-}NH_2)_6$).[6] In a typical synthesis, 3 mmol of 1,4-bis(1H-pyrazol-4-yl)benzene (H_2BDP, 630.99 mg) or the amino derivative ($H_2BDP\text{-}NH_2$, 675.75 mg) were dissolved in 160 mL of *N*,*N*-dimethylformamide (DMF) and 4 mmol (992 mg) of $Ni(AcO)_2\cdot 4H_2O$ were dissolved in 40 mL of H_2O. The two limpid solutions were mixed and refluxed overnight under stirring. The resulting light green solid was filtered and washed with ethanol (EtOH) and diethyl ether (Et_2O). The solid was then refluxed with DMF for 2 h and filtered. The solid was stirred in dichloromethane (CH_2Cl_2) for 2 h at RT and filtered. Ni_8BDP_6 and $Ni_8(BDP\text{-}NH_2)_6$ samples were evacuated for 12 h at 150 ºC.

KOH@Ni_8BDP_6 or $K[Ni_8(OH)_5(C_2H_5O)_2(H_2O)_2(C_{12}H_8N_4)_{5.5}]\cdot n(H_2O)$, (KOH@$Ni_8BDP_6$).[7] First of all, Ni_8BDP_6 was thermally activated at 150 ºC and outgassed, in order to obtain the evacuated porous matrix. Afterwards, 0.055 mmol (100 mg) was suspended in a 0.35 M KOH absolute ethanol solution (5.5 mL). The resulting suspension was stirred overnight under an inert N_2 atmosphere, filtered off and copiously washed with absolute ethanol, yielding to KOH@Ni_8BDP_6. Finally, KOH@Ni_8BDP_6 was evacuated for 12 h at 150 ºC.

UiO-66 and UiO-66-NH_2 or $[Zr_6O_4(OH)(C_8H_3O_4X)_6]\ nH_2O$, X = H (UiO-66) or NH_2 (UiO-66-NH_2).[8,9] 1 mmol of $ZrCl_4$ (233.03 mg) and 1 mmol of dicarboxylic linker (terephthalic acid, H_2BDC, 166.13 mg; or 2-aminoterephthalic acid, $H_2BDC\text{-}NH_2$, 181.15 mg) were dispersed in 3 mL of DMF, placed in a teflon-lined autoclave and heated for 12 h at 220 °C (UiO-66) or 24 h at 100 ºC (UiO-66-NH_2). The resulting solid was recovered by filtration and washed with deionized water and acetone. 200 mg of the solid were suspended in 100 mL of DMF under stirring for 12 h. Then, the DMF-washed solid was suspended in 100 mL of methanol (MeOH)

under stirring for 12 h, recovering the activated solid by filtration. UiO-66 and UiO-66-NH_2 samples were evacuated for 12 h at 200 °C and 150 ºC, respectively.

MIL-163 or $[Zr_2(C_{14}H_2O_6N_4)_2]\cdot(DMA)_5(H_2O)_{14}$*, DMA: N,N-dimethylamine.*[4] In a 25 mL teflon-lined steel autoclave, 0.2 mmol (47 mg) of $ZrCl_4$ was added to a solution of 0.4 mmol of the 5,5'-(1,2,4,5-tetrazine-3,6-diyl)bis(benzene-1,2,3-triol) ligand (H_6-TzGal, 132 mg) in DMA (2 mL) at RT. Water (3 mL) was then added under stirring, and the autoclave sealed and placed in the oven for 24 h at 130 ºC. After cooling to RT, the solution was filtered and MIL-163 was recovered as a dark-red fine powder. The solid was then washed in DMF (10 mL) and EtOH (10 mL) for one night with each, before being filtered and dried in air.

MIL-127 or $[Fe_3O(OH)_{0.88}Cl_{0.12}(C_{16}N_2O_8H_6)_{1.5}(H_2O)_3]\cdot nH_2O$.[10] The solution obtained by adding 0.927 g of NaOH to 26 mL of propan-2-ol in a 250 mL round-bottom flask, was stirred until complete dissolution of NaOH. After the addition of 10.1 mmol (3.636 g) of 3,3',5,5'-azobenzenetetracarboxylic acid ligand (H_4-TazBz), the resulting solution was stirred at 90 °C. In parallel, 20 mmol (5.498 g) of $FeCl_3\cdot 6H_2O$ were dissolved in 14 mL of propan-2-ol in a flask at 70 °C. In the next step, a mixture obtained by mixing the iron and the ligand solutions was stirred under reflux for 24 h. A crystalline powder was recovered by filtration, washed with 200 mL of distilled water (to remove Na salts), 200 mL of propan-2-ol, and finally with 200 mL of ethanol. MIL-127 was evacuated for 12 h at 150 ºC.

MIL-53 or $[Fe(OH)(C_8O_4H_4)]\cdot H_2O$.[11] In a typical synthesis, 0.1 mol (27 g) of $FeCl_3.6H_2O$ and 0.1 mol (16.6 g) of H_2BDC were dispersed in 500 mL of DMF. The mixture was placed in a round bottom flask and refluxed for 48 h at 150 °C under stirring. Then, the yellow solid was recovered by filtration and washed with DMF. Then, the solid was suspended in 500 mL of water for 12 h. MIL-53 was evacuated for 12 h at 200 °C.

MIL-53-$(OH)_2$ *or* $[Fe(OH)(C_8H_4O_6)]\cdot n(DMF)$.[12] 6.8 mol (1.34 g) of 2,5-dihydroxyterephthalic acid (H_2BDC-$(OH)_2$), 4.6 mol (1.63 g) of $Fe(ClO_4)_3\cdot H_2O$, 25 mL of DMF, 1 mL of a 5 M hydrofluoric acid solution and 5 mL of a 5 M perchloric acid solution were placed in a 125 mL teflon-lined steel autoclave. The mixture stirred for 10 minutes, the autoclave sealed, and placed in an oven at 100 °C for 16 h. Crude MIL-53-$(OH)_2$ was recovered as a dark crystalline solid by filtration, washed with ethanol and dried in air. MIL-53-$(OH)_2$ sample was evacuated for 12 h at 130 °C.

S4. Atenolol adsorption studies

Adsorption and stability studies. Prior to the At adsorption studies, the stability of the isolated At in water was confirmed by HPLC for at least 24 h, ruling out the formation of any byproduct that can distort the quantification or compete in the At adsorption process. At adsorption studies were performed by suspending 30 mg of desolvated MOFs in 30 mL of tap water (pH = 7.3) containing different amount of At. The MOF:At molar ratios were 1:2 and 1:0.5, using At concentration from 0.08 to 2245.6 $mg \cdot L^{-1}$. It has to be pointed that this concentration is in the range of the reported concentration of At in river waters.[13,14]

The suspensions were stirred under bidimensional continuous stirring (80 x 80 rpm) at 25 ºC for 24 h. At different incubation times, the suspensions were centrifuged (14500 rpm, 10 min), and filtered with a syringe filter (0.2 μm) to obtain clean solutions. The obtained solids were characterized by XRPD to check their crystallinity, while the liquid phases were analyzed by HPLC, determining the amount of At and the total amount of possible MOF's leached ligand in the solution. A further study was performed using At aqueous solutions prepared with real water samples (from Manzanares river-Madrid, Spain, collected in March 2018, pH = 6.0). Before its use, Manzanares water was filtered (0.2 μm filter) to remove the solid content. All the At studies and leached ligand determinations were performed by triplicate.

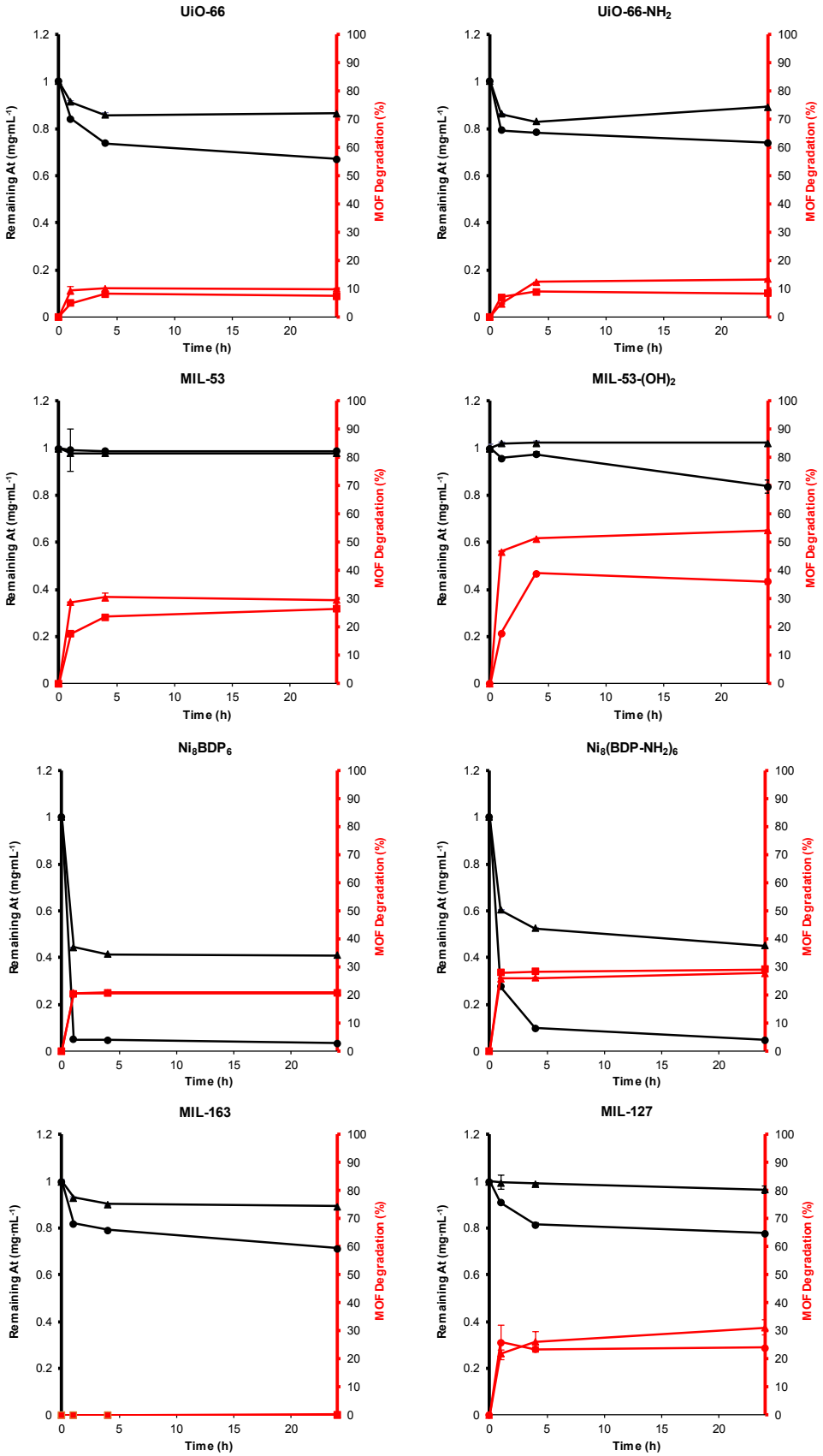

Figure S9. Effect of adsorption times on the remaining At (black, left) and ligand leaching (red, right) over different MOFs. Two different MOF:At molar ratios have been studied (1:0.5, circles; 1:2, triangles). To facilitate comparison between MOFs, the initial At concentration has been normalized to 1 mg·mL^{-1}.

Table S1. Pores, channels and molecules dimensions (Å), Brunauer, Emmett and Teller surface areas (S_{BET}, $m^2 \cdot g^{-1}$), pore volume (V_p, $cm^3 \cdot g^{-1}$), MOF:At molar ratio, total At loading at the plateau (adsorption capacity at equilibrium, q_e, mg of At$\cdot g^{-1}$ of material); At adsorbed ($mol \cdot mol^{-1}$), removal of At with respect to the initial concentration (%), and MOF degradation (%) for all studied materials.

Structure	**Dimensions (porosity or molecule size, Å)**	**S_{BET} ($m^2 \cdot g^{-1}$) V_p ($cm^3 \cdot g^{-1}$)**	**Ratio (MOF:At)**	**q_e ($mg \cdot g^{-1}$)**	**Adsorbed At ($mol \cdot mol^{-1}$)**	**Adsorbed At (%)**	**MOF degradation (%)**
At	15 x 7 x 5 $Å^3$	-	-	-	-	-	-
Ni_8BDP_6	Td (9 Å) and Oh (16 Å) cages accessible via triangular windows (6 – 12 Å)	1300 0.54	1:2 1:0.5	174.85 71.61	1.20 ± 0.01 0.49 ± 0.00	59.16 ± 0.12 97.00 ± 0.02	21.10 ± 0.11 20.58 ± 0.09
$Ni_8(BDP\text{-}NH_2)_6$		1138 0.40	1:2 1:0.5	154.97 66.16	1.06 ± 0.01 0.45 ± 0.00	55.00 ± 0.00 95.39 ± 0.02	27.72 ± 0.19 29.04 ± 0.04
UiO-66	Td (8 Å) and Oh (11 Å) cages accessible via triangular windows (5 - 7 Å)	1162 0.50	1:2 1:0.5	49.88 29.61	0.31 ± 0.02 0.19 ± 0.00	13.59 ± 0.47 33.04 ± 0.01	9.91 ± 0.04 7.40 ± 0.53
UiO-66-NH_2		610 0.29	1:2 1:0.5	35.91 20.47	0.24 ± 0.00 0.14 ± 0.01	10.77 ± 0.07 26.15 ± 0.19	13.33 ± 0.13 8.26 ± 0.02
MIL-163	Square shaped channels 12 x 12 Å	90-170[c]	1:2 1:0.5	128.13 92.24	0.22 ± 0.00 0.16 ± 0.00	10.63 ± 0.34 28.64 ± 0.06	0.09 ± 0.00 0.06 ± 0.01
MIL-127	1D channels (6 Å) and cages (10 Å) accessible via narrow apertures (3 Å)	1304 0.7	1:2 1:0.5	26.31 42.73	0.08 ± 0.03 0.13 ± 0.00	3.57 ± 1.52 22.30 ± 0.13	31.20 ± 2.71 24.11 ± 0.31
MIL-53	7.5 Å (hydrated)[d]	-	1:2 1:0.5	41.50 7.10	0.04 ± 0.00 0.01 ± 0.00	2.25 ± 0.2 1.15 ± 0.16	29.56 ± 0.01 26.43 ± 0.03
MIL-53-$(OH)_2$	9.1 Å (hydrated)[d]	-	1:2 1:0.5	0 88.94	0.00 ± 0.00 0.09 ± 0.02	0 ± 0.68 16.27 ± 0.03	54.14 ± 0.33 36.10 ± 1.00
Activated charcoal (Norit)	6.5 and 13.5 Å[a]	620 0.2	30.00:29.19 30.00:7.30[b]	61.65 73.75	0.002 ± 0.000 0.003 ± 0.000	21.40 ± 0.03 91.33 ± 0.01	-

[a] Pore size distribution determined using the density functional theory method (DFT).[15]
[b] For comparison reasons and due to the difference on MOFs and carbon molecular weights, here the activated charcoal:At ratio is expressed in mass (mg).
[c] Flexible matrix confirmed by a low N_2 adsorption compare to the expected from the structural analysis.
[d] Pore size determinations using crystal structure of hydrated forms (considering distances and Van der Waals raddi).

S5. MOFs stability

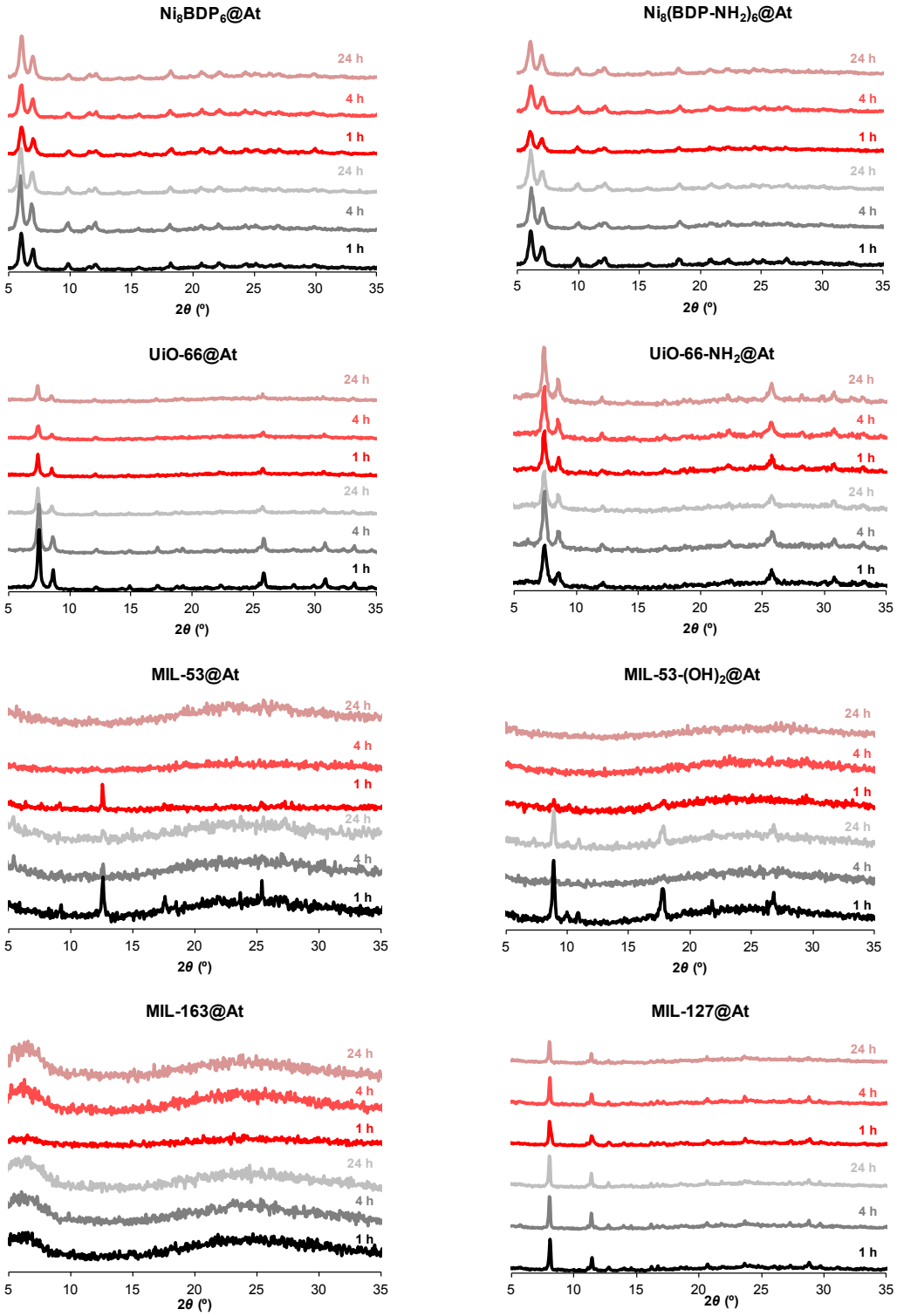

Figure S10. XRPD patterns for all MOF after been suspended in tap At solutions with different MOF:At ratios (1:2, red; and 1:0.5, black) for 1, 4 and 24 h under stirring at room temperature.

S6. KOH@Ni_8BDP_6 material: improved At adsorption

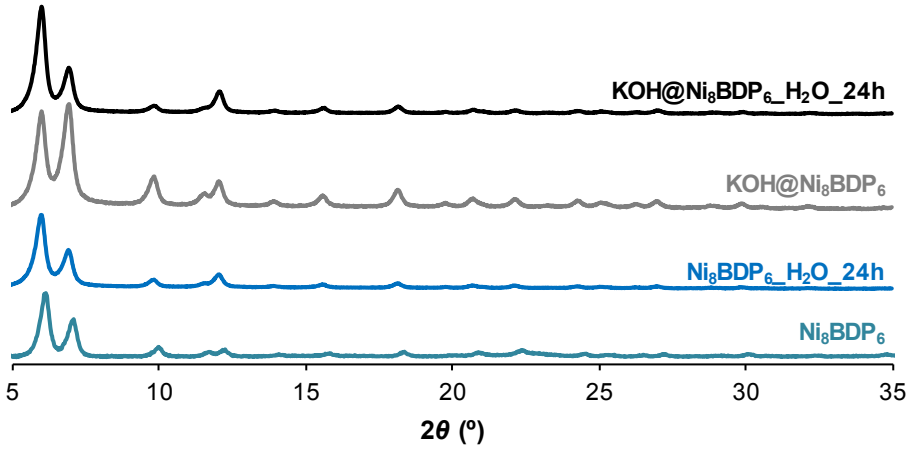

Figure S11. XRPD patterns for Ni_8BDP_6 and KOH@Ni_8BDP_6 before and after been suspended in tap water for 24 h at room temperature.

FTIR spectra of both At-loaded materials confirmed the presence of bands of At corresponding to its aromatic ring in the loaded materials. Further, bands of At characteristic of the ν(C-H)$_{ring}$ and w(C-H)/δ(C-H)$_{ring}$ are shifted in the loaded materials from 1512 to 1510 cm^{-1} and 1298 to 1292 cm^{-1}, respectively,[16] suggesting the formation of π-π stacking interactions between the At ring and the framework. Further, the characteristic bands of the At amide (ν(N-H): 3346 and 3155 cm^{-1}; ν(C=O): 1656 cm^{-1}; and δ(NH): 1634 cm^{-1}) are strongly shifted in the At-loaded Ni_8BDP_6 (ν(N-H): 3462 and 3356 cm^{-1}, ν(C=O): 1682 cm^{-1}, and δ(NH): 1666 cm^{-1}) and KOH@Ni_8BDP_6 (ν(N-H): 3460 and 3357 cm^{-1}, ν(C=O): 1680 cm^{-1}, and δ(NH): 1666 cm^{-1}, respectively, Fig S13). One could hypothesize the formation of specific interactions between the At-amide and reactive group of the MOFs, such as metal Ni sites, Ni-OH and Ni-OH_2.

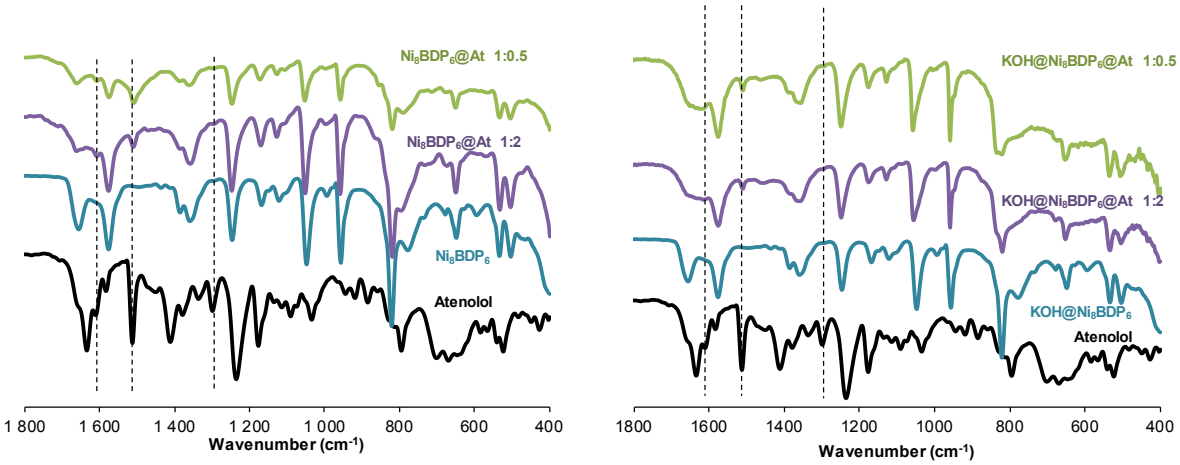

Figure S12. FTIR spectra of At, pristine Ni_8BDP_6, KOH@Ni_8BDP_6, and At loaded materials obtained using different MOF:At ratio. The wavenumbers and the description of the main peaks of At found in the loaded matrixes are 1610 cm^{-1} (ν(C=C) ring), 1512 cm^{-1} (ν(C-H) ring), and 1296 cm^{-1} (w(C-H) and δ(C-H) ring).

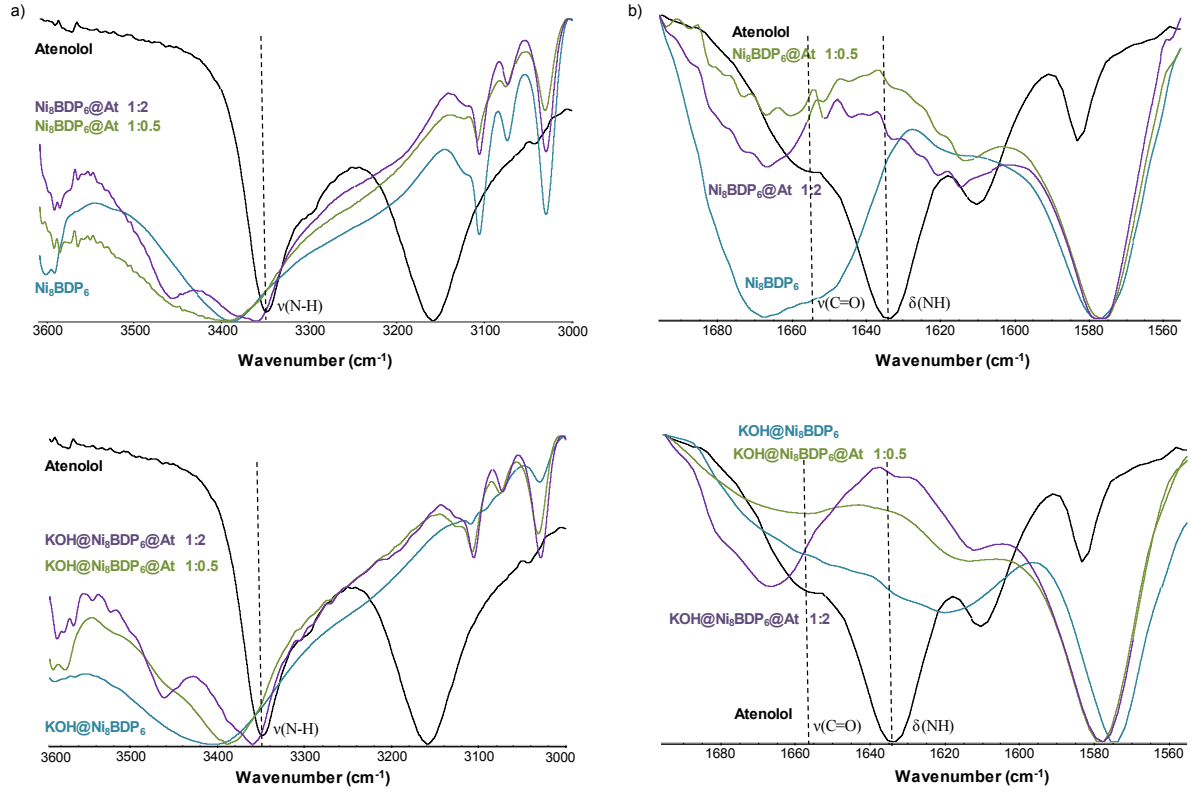

Figure S13. Local enlargement of the characteristic bands of amide present in At from 3600 to 3000 cm^{-1} (a) and 1700 to 1550 cm^{-1} (b) of the FTIR spectra of At, pristine Ni_8BDP_6 (top) and KOH@Ni_8BDP_6 (bottom) and At loaded materials obtained using different MOF:At ratio. It should be noted that as water absorption bands are on the range of 3500 – 3100 cm^{-1} all the FTIR spectra were obtained using KBr pellets previously dried at 100 ºC overnight.

XRPD patterns of the At-containing KOH@Ni_8BDP_6 evidenced that the At loading process does not alter the crystalline structure of the porous materials. It has to be highlighted again the exceptional stability of KOH@Ni_8BDP_6 with an almost negligible linker leaching after 24 h (0.06 % in ratio 1:2 studies; and 0.11% using in ratio 1:0.5 studies).

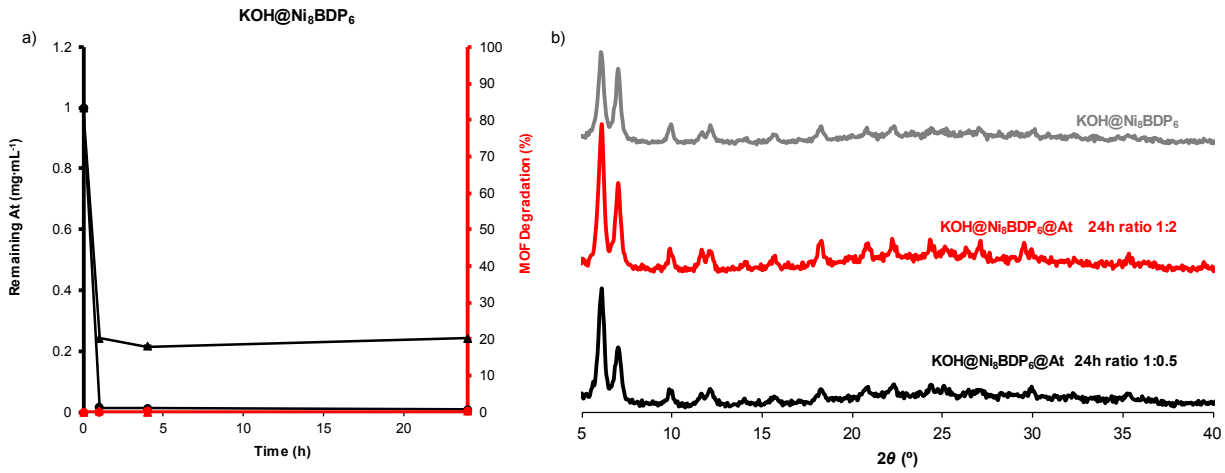

Figure S14. (a) Evolution of At removal (a, in black) using two different KOH@Ni_8BDP_6:At ratios (1:2, triangles; 1:0.5, circles) for 24 h under stirring at RT. The concentration of At has been normalized for an easier comparison. The matrix degradation was also represented (a, in red). (b) XRPD patterns of KOH@Ni_8BDP_6 before and after been suspended in At water tap solutions.

Table S2. Textural properties (S_{BET} in $m^2 \cdot g^{-1}$ and V_p in $cm^3 \cdot g^{-1}$), MOF:At ratio, total At loading at the plateau (adsorption capacity at equilibrium, q_e, mg of At$\cdot g^{-1}$ of material), adsorbed At ($mol \cdot mol^{-1}$), removal of At with respect to the initial concentration (%), and MOF degradation (%) before and after At adsorption process.

MOF	S_{BET} ($m^2 \cdot g^{-1}$)	V_p ($cm^3 \cdot g^{-1}$) Occupation (%)	Ratio (MOF:At)	q_e ($mg \cdot g^{-1}$)	Adsorbed At ($mol \cdot mol^{-1}$)	Adsorbed At (%)	MOF degradation (%)
Ni_8BDP_6	1300	0.54	1:2 1:0.5	-	-	-	-
Ni_8BDP_6@At	776 1049	0.32 (40.7) 0.48 (11.1)	1:2 1:0.5	174.85 71.61	1.20 ± 0.01 0.49 ± 0.00	59.16 ± 0.12 97.00 ± 0.02	21.10 ± 0.11 20.58 ± 0.09
KOH@Ni_8BDP_6	1502	0.61	-	-	-	-	-
KOH@Ni_8BDP_6@At	817 1126	0.34 (44.3) 0.47 (22.9)	1:2 1:0.5	255.51 76.78	1.76 ± 0.00 0.53 ± 0.00	91.86 ± 0.02 99.94 ± 0.01	0.06 ± 0.05 0.12 ± 0.04
Activated charcoal (Norit)	624	-	1:2 1:0.5	61.65 73.75	0.002 ± 0.000 0.003 ± 0.000	21.40 ± 0.03 91.33 ± 0.01	-

S7. Ni_8BDP_6 and KOH@Ni_8BDP_6: a detailed study

When Ni_8BDP_6 is exposed to aqueous solutions at different pH, its ζ-potential remains neutral in almost the entire pH range (from 1 to 7 and from 11 to 12), becoming negative at pH from 7 to 10. On the other hand, KOH@Ni_8BDP_6 is positively charged under acidic conditions (pH < 4), neutral (from 4 to 7), and negative (pH > 7). Thus, the main difference between the superficial charge of both materials is found at low pH (< 4), being neutral for Ni_8BDP_6 and positive for KOH@Ni_8BDP_6. In this regard, the postsynthetic removal of organic linkers (within the framework and on the surface) may lead to the formation of accessible extra Ni^{2+} sites (according to the Pourbaix diagram),[45] resulting in framework degradation at very acidic pH. On the other hand, under strong basic conditions (pH > 10), one could propose several effects explaining the differences found between Ni_8BDP_6 and KOH@Ni_8BDP_6: *i)* the deprotonation of the OH groups (Ni-OH/NiO^-; pK_a ~ 10), *ii)* creation of defects, associated with the formation of Ni-OH, and *iii)* the substitution of the extraframework electropositive K^+ in KOH@Ni_8BDP_6 by the less electropositive Na^+ (coming from the NaOH titrant).

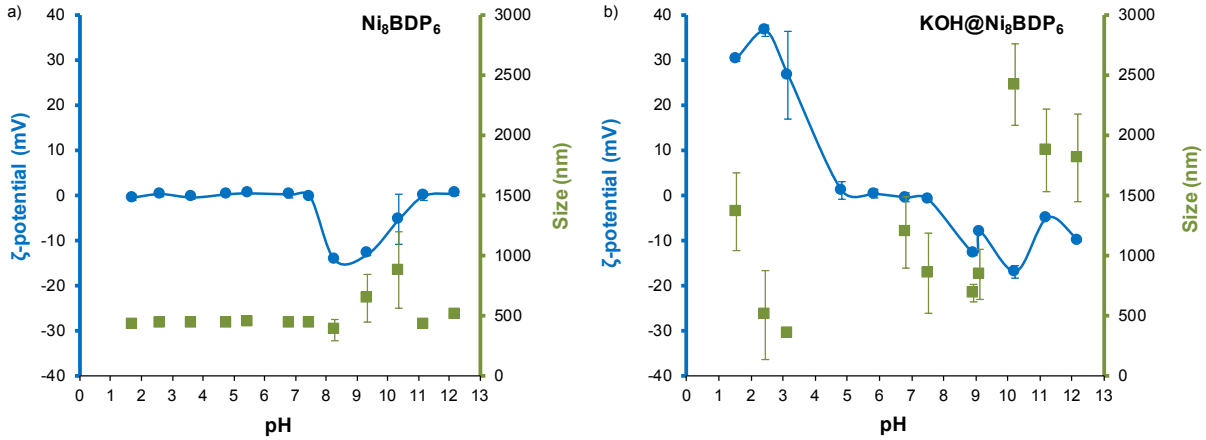

Figure S15. Evolution of particle size (left, green) and ζ-potential (right, blue) of (a) Ni_8BDP_6 and (b) KOH@Ni_8BDP_6 materials as function of pH.

TEM images show tetragonal particles with mean sizes of *ca*. 14 nm (n = 250) for both materials. The presence of extraframework K^+ (associated with linker defects) was confirmed by EDX elemental mapping (Ni, N, O, and K), demonstrating a homogeneous distribution around the KOH@Ni_8BDP_6 particles.

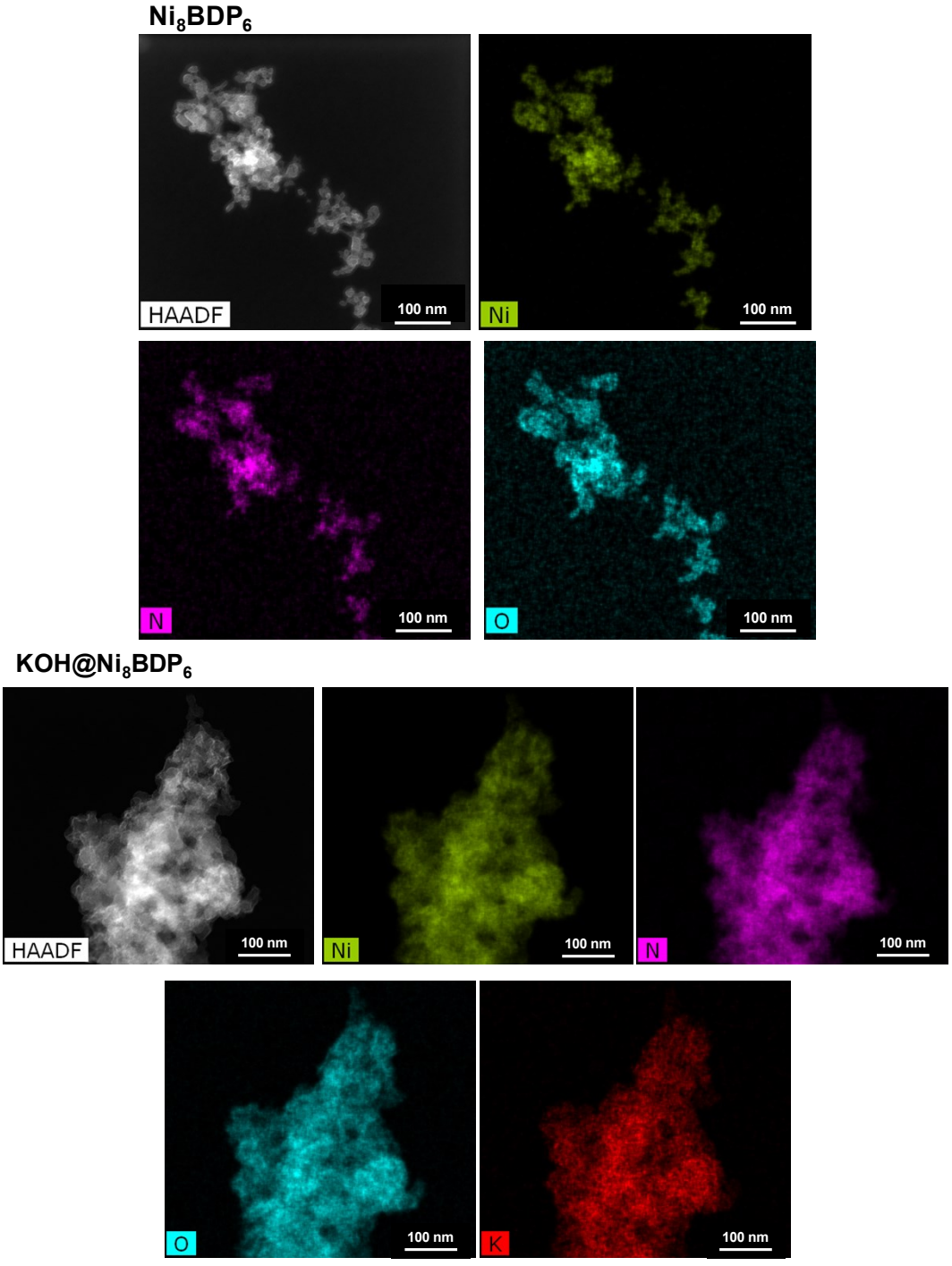

Figure S16. Elemental mapping obtained by EDX of the Ni based porous materials Ni_8BDP_6 and KOH@Ni_8BDP_6. The presence of Ni, N, O, and K elements into particles is confirmed.

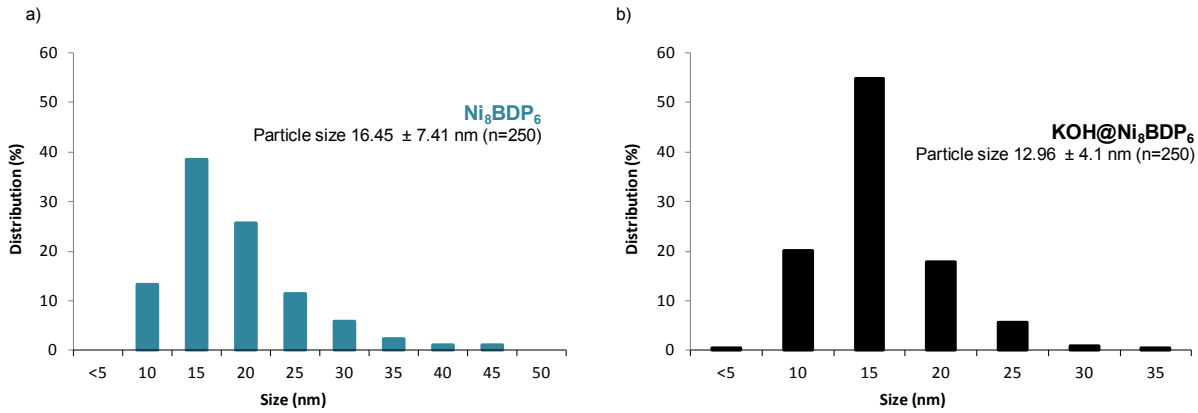

Figure S17. Particle size distribution (nm) of (a) Ni_8BDP_6 and (b) KOH@Ni_8BDP_6.

S8. Continuous water purification studies

First, pellets of Ni_8BDP_6 and KOH@Ni_8BDP_6 were prepared and their stability was studied in water. 70 mg of the original sample were pelletized by the application of a pressure up to 0.15 GPa (1.5 tons cm^{-2}) for 1 minute. The as-prepared pellets were suspended in water for 24 h under bidimensional continuous stirring (80 x 80 rpm) at room temperature. No loss of crystallinity was observed, while the N_2 sorption capacity was maintained.

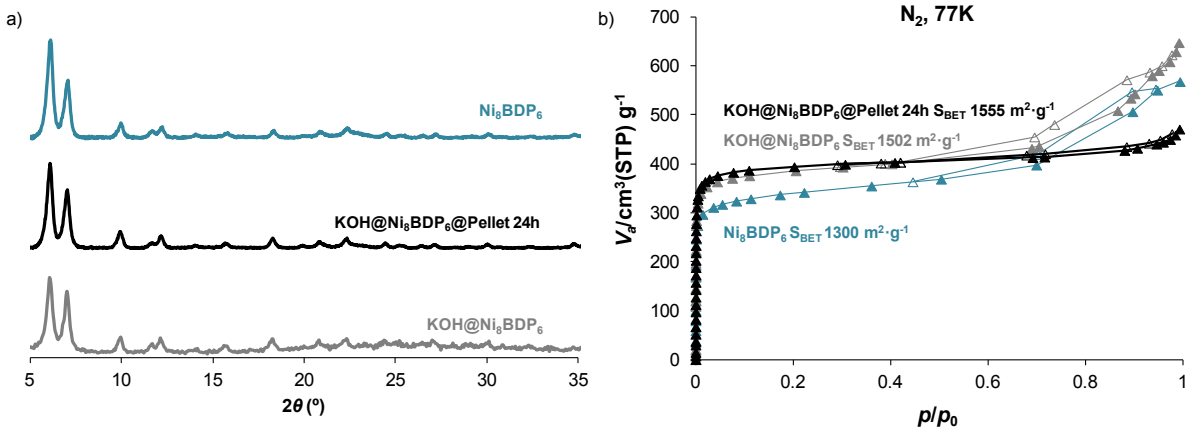

Figure S18. (a) XRPD patterns and (b) N_2 adsorption isotherms of original Ni_8BDP_6 and KOH@Ni_8BDP_6 materials, and KOH@Ni_8BDP_6@Pellet after been suspended in water for 24 h at room temperature.

Continuous flow At adsorption. A fixed bed column made of plastic tube (internal diameter Ø = 1.5 cm, length = 4.7 cm) was employed to monitor At removal through a continuous flow system. In order to provide a suitable liquid distribution and avoid overpressure, small pieces of KOH@Ni_8BDP_6 pellets (*ca.* ≤ 5 mm) and glass wool was used to fix the MOF bed. KOH@Ni_8BDP_6 pellets (column dimensions: 1.2 cm Ø, 1.08 cm height) were prepared from pure powder sample by applying pressure (15000 tons for 1 minute) to 70 mg of powdered sample. 400 mg of KOH@Ni_8BDP_6 pellets were utilized. The dead volume inside the column was negligible. Before any test, the column was previously conditioned with 60 mL of tap water. The At adsorption studies were performed using a NE-4000 dual-channel syringe (Micrux, Spain) pumping system with a continuous flow of 100 µL·min^{-1} (equivalent to *ca.* 34 L·m^{-2}·h^{-1}) using three different At concentrations (73, 146 and 250 mg·L^{-1}) in tap water. Note here that the concentration is on the range or higher than the At found in previously analyzed river waters; from 0.35 to 2.21 mg·L^{-1}.[13,14] Aliquots of 100 µL (pH = 7.5) were collected at different time intervals and the At and H_2BDP concentrations were analyzed to study the At adsorption and potential MOF degradation in a continuous mode. A blank with glass wool was

also tested, with no signs of At adsorption. The continuous flow study was performed by triplicate.

Regeneration of KOH@Ni$_8$BDP$_6$. The regeneration of KOH@Ni$_8$BDP$_6$ as adsorbent was test by soaking the At loaded KOH@Ni$_8$BDP$_6$@At in different solvents (*i.e.* methanol, acetone, ethanol, dichloromethane). Unfortunately, no adsorption capacity recovery was achieved.

The breakthrough curve shape and the time to reach breakthrough are considered as the main factors to investigate the efficiency of the fixed-bed adsorption column. Prediction of the breakthrough curves for the effluent is a requisite for the accurate design of a continuous adsorption column.[17] In this study, a non-linear model was employed to describe the continuous adsorption system (Origin Pro 2019b software was used for non-linear curve fitting).

The Thomas model is one of the most general and widely utilized theoretical methods to describe column performance and it is described following equation 1:[19]

$$\ln\left(\frac{C_0}{Ct}-1\right)=\frac{K_{Th}q_oM}{F}-K_{Th}C_0t \qquad \text{(eq.1)}$$

where C_0 is the inlet At concentration (mg·L^{-1}); Ct is the effluent At concentration at time (mg·L^{-1}); K_{Th} is the Thomas rate constant (mL·mg^{-1}·min^{-1}); q_o is the equilibrium of At uptake (mg·g^{-1}); M is the mass of the absorbent (g); F is the inlet flow rate (mL·min^{-1}); and t is the flow time (min).

The Thomas model, considering Langmuir kinetics of adsorption-desorption and no axial dispersion, is derived with the assumption that the rate driving force obeys second-order reversible reaction kinetics.[22] The continuous flow data were fitted to this model using non-linear regression in order to determine the characteristic parameters of the column that are useful for process design. Further, and in order to compare the effect of changing At concentration in the feeding solution, the adsorbed amount of At (q_e) was calculated by integrating the area of the breakthrough curves using the following equation 2:

$$q_e=\frac{C_0F\int_0^t\left(1-\frac{C}{C_0}\right)}{F} \qquad \text{(eq. 2)}$$

DFT adsorbate location. In order to localize the adsorption capacity and location of At in the pores of Ni$_8$BDP$_6$ and KOH@Ni$_8$BDP$_6$ systems, we have employed the Adsorption Locator module of the Materials Studio 6.0 software [Biovia Materials Studio 6.0: San Diego: Dassault

Systèmes 2018] to perform Monte Carlo simulations. The used forcefield was COMPASS,[20] the charge was forcefield assigned and the summation methods were group- and atom-based. The simulations yielded the most stable conformations of At molecules within the pores of the studied Ni_8BDP_6 and $KOH@Ni_8BDP_6$ systems.

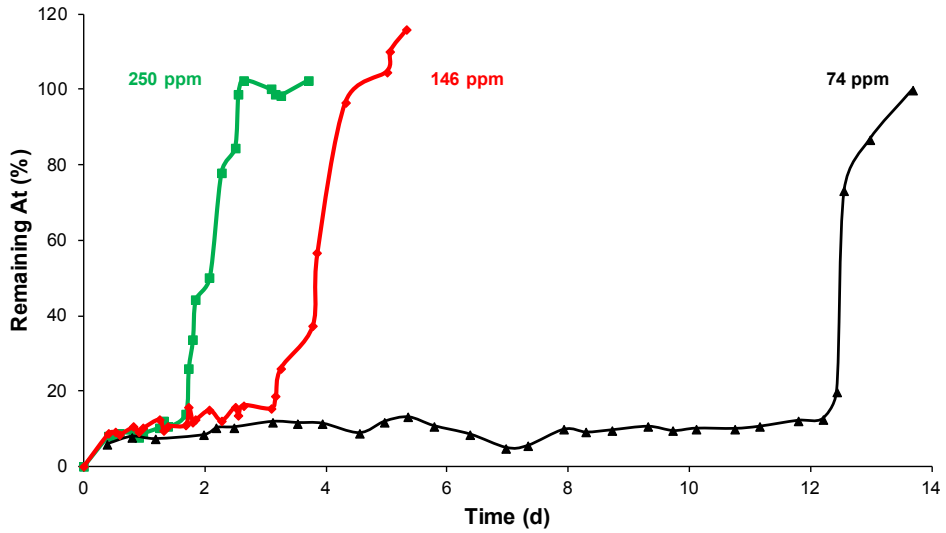

Figure S19. The effect of the concentration of the inlet flow on the breakthrough curve of At sorption.

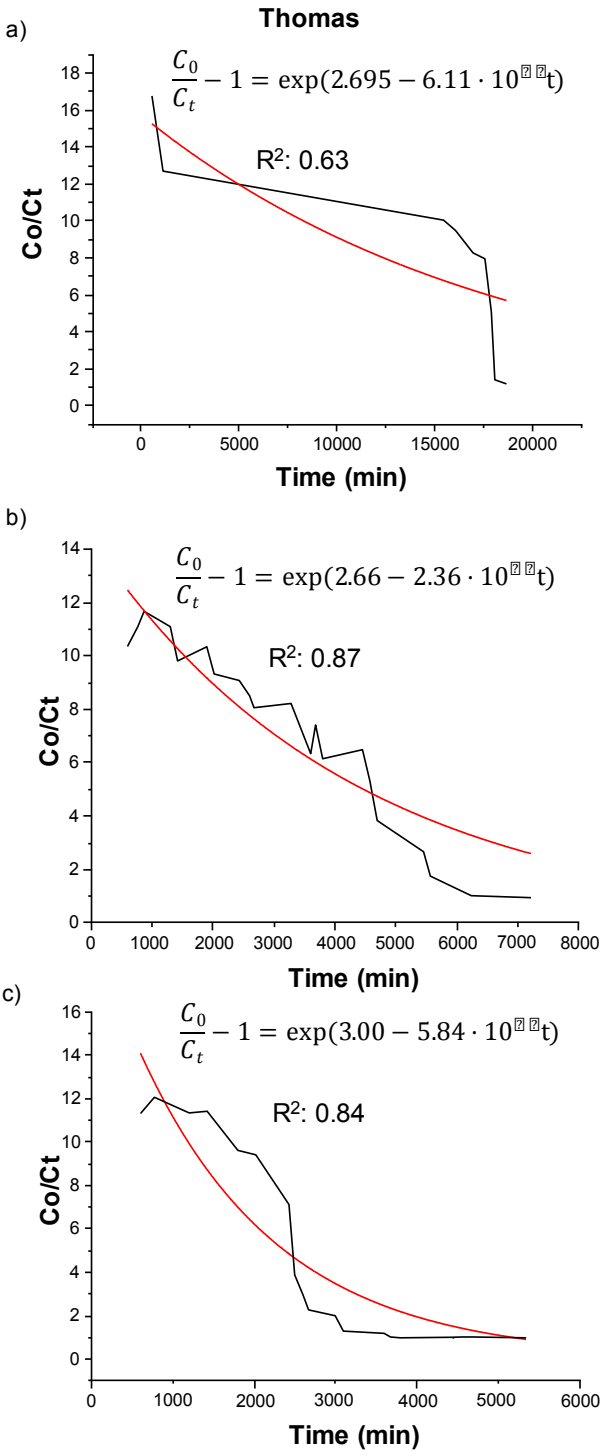

Figure S20. Breakthrough curves and fitting of the data from the continuous water purification studies using the Thomas model using different inlet concentrations: (a) 73 ppm, (b) 146 ppm, and (c) 250 ppm.

Table S3. Experimental conditions and parameter of Thomas model under different conditions based on non-linear regression analysis. Initial concentration (C_0), amount of At adsorbed (q_e), and kinetic constant calculated using Thomas model (K_{Th}).

C_0 (mg·L^{-1})	Volume (mL)	Time (days)	Degraded MOF (%)	K_{Th} (mL·mg^{-1}·min^{-1})	q_e (mg·g^{-1})
73	2120	12.2	3.73	$8.37 \cdot 10^{-4}$	56.53
146	760	3.1	3.49	$1.62 \cdot 10^{-3}$	15.71
250	535	1.7	3.09	$2.34 \cdot 10^{-3}$	6.29

Table S4. Operating conditions (flow rate in L·m^{-2}·h^{-1}, column volume in cm^3 and dimensions in cm, contact time in h, initial concentration of contaminant (*Co*) in mg·L^{-1}) and parameters of the breakthrough analysis (breakthrough time in min, kinetic constant *(K)* in mL·min^{-1}·mg^{-1}, and model used**)** of different MOFs used in the adsorption of PPCPs and activated carbon used in the At adsorption. For an easy comparison, operation conditions in water treatment plants are also indicated.

MOF + contaminant	Flow rate / column volume (L·m^{-2}·h^{-1} / cm^3)	Column dimensions (cm)	Contact or Residence time (h)	*Co* (mg ·L^{-1})	Breakthrough time (min)	*K* (mL·min^{-1}·mg^{-1})	Model used	Ref.
ZIF-8 + oxytetracycline	58 0.29	Ø: 0.58 Height: 1.1	-	40	200	-	Not defined	[23]
MIL-101(Cr) + diazinon	764 0.78	Ø: 1 Height: 1	-	100	8	$6.21 \cdot 10^{-4}$	Thomas	[24]
Granular activated carbon + atenolol	1593 8.48	Ø: 0.6 Height: 30	-	0.5	*ca.* 600	$1.5 \cdot 10^{-3}$	Thomas	[25]
KOH@Ni_8BDP_6 + atenolol	34 1.13	Ø: 1.2 Height: 1.08	0.41	73	43 200	$8.37 \cdot 10^{-4}$ $1.18 \cdot 10^{-2}$	Thomas A-B	This study
Water treatment plants	27 – 530000 / (10^{-7} - $5 \cdot 10^7$	$5 \cdot 10^4$ - $30 \cdot 10^4$ Ø, 180 - 400	0.08 - 9					[26]

S9. References

(1) Colombo, V.; Montoro, C.; Maspero, A.; Palmisano, G.; Masciocchi, N.; Galli, S.; Barea, E.; Navarro, J. A. R. Tuning the Adsorption Properties of Isoreticular Pyrazolate-Based Metal − Organic Frameworks through Ligand Modification. *J. Am. Chem. Soc.* **2012**, *134*, 12830–12843. https://doi.org/10.1021/ja305267m.

(2) Lozan, V.; Solntsev, P. Y.; Leibeling, G.; Domasevitch, K. V; Kersting, B. Tetranuclear Nickel Complexes Composed of Pairs of Dinuclear LNi2 Fragments Linked by 4,4 ′-Bipyrazolyl, 1,4-Bis(4′-Pyrazolyl)Benzene, and 4,4′-Bipyridazine: Synthesis, Structures, and Magnetic Properties. *Eur. J. Inorg. Chem.* **2007**, 3217–3226. https://doi.org/10.1002/ejic.200700317.

(3) Maspero, A.; Galli, S.; Masciocchi, N.; Parmisano, G. Facile Preparation of Polytopic Azoles: Synthesis, Characterization, and X-Ray Powder Diffraction Studies of 1,4-Bis(Pyrazol-4-Yl)- and 1,4-Bis(Tetrazol-5-Yl)Benzene. *Chem. Lett.* **2008**, *37*, 956–957. https://doi.org/10.1246/cl.2008.956.

(4) Mouchaham, G.; Cooper, L.; Guillou, N.; Martineau, C.; Elkaïm, E.; Bourrelly, S.; Llewellyn, P. L.; Allain, C.; Clavier, G.; Serre, C.; et al. A Robust Infinite Zirconium Phenolate Building Unit to Enhance the Chemical Stability of Zr MOFs. *Angew. Chem. Int. Ed. Engl.* **2015**, *54*, 13297–13301. https://doi.org/10.1002/anie.201507058.

(5) Dhakshinamoorthy, A.; Alvaro, M.; Chevreau, H.; Horcajada, P.; Devic, T.; Garcia, H. Iron(III) Metal–Organic Frameworks as Solid Lewis Acids for the Isomerization of Alfa-Pinene Oxide. *Catal. Sci. Technol.* **2012**, *3*, 324–330. https://doi.org/10.1039/c2cy00376g.

(6) Padial, N. M.; Quartapelle Procopio, E.; Montoro, C.; López, E.; Oltra, J. E.; Colombo, V.; Maspero, A.; Masciocchi, N.; Galli, S.; Senkovska, I.; et al. Highly Hydrophobic Isoreticular Porous Metal-Organic Frameworks for the Capture of Harmful Volatile Organic Compounds. *Angew. Chem. Int. Ed. Engl.* **2013**, *52* (32), 8290–8294. https://doi.org/10.1002/anie.201303484.

(7) López-Maya, E.; Montoro, C.; Colombo, V.; Barea, E.; Navarro, J. A. R. Improved CO2 Capture from Flue Gas by Basic Sites, Charge Gradients, and Missing Linker Defects on Nickel Face Cubic Centered MOFs. *Adv. Funct. Mater.* **2014**, *24*, 6130–6135. https://doi.org/10.1002/adfm.201400795.

(8) Cavka, J. H.; Jakobsen, S.; Olsbye, U.; Guillou, N.; Lamberti, C.; Bordiga, S.; Lillerud, K. P. A New Zirconium Inorganic Building Brick Forming Metal Organic Frameworks with Exceptional Stability. *J. Am. Chem. Soc.* **2008**, *130*, 13850–13851. https://doi.org/10.1021/ja8057953.

(9) Kandiah, M.; Nilsen, M. H.; Usseglio, S.; Jakobsen, S.; Olsbye, U.; Tilset, M.; Larabi, C.; Quadrelli, E. A.; Bonino, F.; Lillerud, K. P.; et al. Synthesis and Stability of Tagged UiO-66 Zr-MOFs. *Chem. Mater.* **2010**, *10*, 6632–6640. https://doi.org/10.1021/cm102601v.

(10) Chevreau, H.; Permyakova, A.; Nouar, F.; Fabry, P.; Livage, C.; Ragon, F.; Garcia-Marquez, A.; Devic, T.; Steunou, N.; Serre, C.; et al. Synthesis of the Biocompatible and Highly Stable MIL-127(Fe): From Large Scale Synthesis to Particle Size Control. *CrystEngComm* **2016**, *18*, 4094–4101. https://doi.org/10.1039/C5CE01864A.

(11) Horcajada, P.; Chalati, T.; Serre, C.; Gillet, B.; Sebrie, C.; Baati, T.; Eubank, J. F.; Heurtaux, D.; Clayette, P.; Kreuz, C.; et al. Porous Metal-Organic-Framework Nanoscale Carriers as a Potential Platform for Drug Delivery and Imaging. *Nat. Mater.* **2010**, *9*, 172–178. https://doi.org/10.1038/nmat2608.

(12) Devic, T.; Horcajada, P.; Serre, C.; Salles, F.; Maurin, G.; Heurtaux, D.; Clet, G.; Vimont, A.; Grene, J.; Ouay, B. Le; et al. Functionalization in Flexible Porous Solids:

Effects on the Pore Opening and the Host-Guest Interactions. *J. Am. Chem. Soc.* **2010**, *132*, 1127–1136. https://doi.org/10.1021/ja9092715.
(13) Lee, H.; Sarafin, K.; Peart, T. E. Determination of B-Blockers and B2-Agonists in Sewage by Solid-Phase Extraction and Liquid Chromatography–Tandem Mass Spectrometry. *J. Chromatogr. A* **2007**, *1148*, 158–167. https://doi.org/10.1016/j.chroma.2007.03.024.
(14) Vieno, N.; Tuhkanen, T.; Kronberg, L. Elimination of Pharmaceuticals in Sewage Treatment Plants in Finland. *Water Res.* **2007**, *41*, 1001–1012. https://doi.org/10.1016/j.watres.2006.12.017.
(15) McCallum, C. L.; Bandosz, T. J.; McGrother, S. C.; Muller, E. A.; Gubbins, K. E. Molecular Model for Adsorption of Water on Activated Carbon: Comparison of Simulation and Experiment. *Langmuir* **1999**, *15* (2), 533–544. https://doi.org/10.1021/la9805950.
(16) de Castro, R. A. E.; Canotilho, J.; Barbosa, R. M.; Redinha, J. S. Infrared Spectroscopy of Racemic and Enantiomeric Forms of Atenolol. *Spectrochim. Acta - Part A Mol. Biomol. Spectrosc.* **2007**, *67* (5), 1194–1200. https://doi.org/10.1016/j.saa.2006.10.007.
(17) Han, R.; Wang, Y.; Zhao, X.; Wang, Y.; Xie, F.; Cheng, J.; Tang, M. Adsorption of Methylene Blue by Phoenix Tree Leaf Powder in a Fixed-Bed Column: Experiments and Prediction of Breakthrough Curves. *Desalination* **2009**, *245* (1–3), 284–297. https://doi.org/10.1016/j.desal.2008.07.013.
(18) Bohart, G. S.; Adams, E. Q. Some Aspects of the Behavior of Charcoal with Respect to Chlorine. *J. Franklin Inst.* **1920**, *189*, 523–544. https://doi.org/10.1016/S0016-0032(20)90400-3.
(19) Rozada, F.; Otero, M.; García, A. I.; Morán, A. Application in Fixed-Bed Systems of Adsorbents Obtained from Sewage Sludge and Discarded Tyres. *Dye. Pigment.* **2007**, *72* (1), 47–56. https://doi.org/10.1016/j.dyepig.2005.07.016.
(20) Sun, H. Compass: An Ab Initio Force-Field Optimized for Condensed-Phase Applications - Overview with Details on Alkane and Benzene Compounds. *J. Phys. Chem. B* **1998**, *102* (38), 7338–7364. https://doi.org/10.1021/jp980939v.
(21) Bohart, G. S.; Adams, E. Q. Some Aspects of the Behavior of Charcoal with Respect to Chlorine. *J. Am. Chem. Soc.* **1920**, *42* (3), 523–544. https://doi.org/10.1021/ja01448a018.
(22) Thomas, H. C. Heterogeneous Ion Exchange in a Flowing System. *J. Am. Chem. Soc.* **1944**, *66* (10), 1664–1666. https://doi.org/10.1021/ja01238a017.
(23) Da Silva, J. D. S. F.; Malo, D. L.; Bataglion, G. A.; Eberlin, M. N.; Ronconi, C. M.; Alves, S.; De Sá, G. F. Adsorption in a Fixed-Bed Column and Stability of the Antibiotic Oxytetracycline Supported on Zn(II)-[2-Methylimidazolate] Frameworks in Aqueous Media. *PLoS One* **2015**, *10* (6), 1–20. https://doi.org/10.1371/journal.pone.0128436.
(24) Mirsoleimani-Azizi, S. M.; Setoodeh, P.; Samimi, F.; Shadmehr, J.; Hamedi, N.; Rahimpour, M. R. Diazinon Removal from Aqueous Media by Mesoporous MIL-101(Cr) in a Continuous Fixed-Bed System. *J. Environ. Chem. Eng.* **2018**, *6* (4), 4653–4664. https://doi.org/10.1016/j.jece.2018.06.067.
(25) Sotelo, J. L.; Ovejero, G.; Rodríguez, A.; Álvarez, S.; García, J. Removal of Atenolol and Isoproturon in Aqueous Solutions by Adsorption in a Fixed-Bed Column. *Ind. Eng. Chem. Res.* **2012**, *51* (13), 5045–5055. https://doi.org/10.1021/ie300334q.
(26) Çeçen, F.; Aktas, O. *Activated Carbon for Water and Wastewater Treatment: Integration of Adsorption and Biological Treatment*; 2011. https://doi.org/10.1002/9783527639441.